Towards Plasma-Induced Swirling Jets

Towards plasma-based swirling jets

Journal of Physics: Conference Series **3063** (2025) 012013 doi:10.1088/1742-6596/3063/1/012013

Towards plasma-based swirling jets

M. Zannone [1], E. Amico [1], P. J. Comunian [1], G. Cafiero [1], G. Iuso [1] and J. Serpieri [1*]

[1]Department of Mechanical and Aerospace Engineering, Politecnico di Torino, Corso Duca degli Abruzzi 24, 10129, Turin

E-mail: *jacopo.serpieri@polito.it

Abstract.

Swirling jets, generated by superimposing an azimuthal velocity component onto a conventional round jet, find widespread utility in industrial applications for their enhanced heat transfer and flame stabilization capabilities. Traditional methods for inducing swirling fluid motions rely on passive techniques, such as guided vanes (e.g. helical inserts) or rotating perforated plates, while emerging approaches, like dielectric barrier discharge plasma actuators (DBD-PAs), offer active control without moving parts. This work emphasizes the performance of passive swirl generators designed to impose predetermined swirl numbers ($S = 0.1, 0.2, 0.3$) and presents a representative active case — employing an array of DBD-PAs — to highlight differences in swirl intensity and flow behaviour between the passive and the active approach. The experimental campaign, conducted using stereoscopic particle image velocimetry, focused on evaluating the induced flow field characteristics. The PAs-induced flow swirl number was compared against the passive cases with known design swirl numbers, using a novel proposed approach. The results hereby discussed indicate that passive methods produce higher swirl numbers ($S = 0.11$–0.29) compared to the active case ($S = 0.08$), due to limitations imposed by the dielectric material used for the PAs embodiment. Radial velocity profiles, vorticity fields, and three-dimensional reconstructions highlight the superior entrainment and uniformity of passive systems, whereas the active configuration exhibits localized tangential velocity generation near the injector walls with minimal impact on the jet core.

1 Introduction

Swirling jets are a class of free shear flows where an azimuthal velocity component is superimposed onto the axial velocity typical of conventional round jet flows. The introduction of a swirl alters the structure and dynamics of the jet in fundamental ways, increasing its spreading rate, turbulence intensity, stability and mixing efficiency. These properties are particularly advantageous in a variety of engineering applications, including combustion systems, spray technologies, and advanced cooling devices [1, 2, 3]. In combustion, swirling flows promote flame stabilization and enhance fuel-air mixing, while in heat exchangers, they improve the convective heat transfer.

The effects of swirl on jet development have been extensively studied. As the swirl intensity increases, the flow undergoes a series of transitions. One of the first phenomena to emerge is the *vortex core precession*, a global instability characterized by a lateral oscillation of the jet core around the axis, resulting from the loss of flow symmetry [4, 5]. This behaviour enhances large-scale mixing and often precedes the formation of a central recirculation zone (CRZ). At even higher swirl numbers, the flow may experience *vortex breakdown*, characterized by a stagnation point followed by a region of reversed flow

along the jet axis [6, 4, 5]. These features, coupled with a rich spectrum of coherent structures, make swirling jets a subject of continued interest in both fundamental and applied fluid dynamics [7].

The flow swirl is typically quantified by a dimensionless parameter known as the swirl number, S. This is generally defined as the ratio between the axial flux of angular momentum and the product of axial momentum flux and nozzle radius. The swirl number depends not only on the magnitude of the azimuthal velocity component but also on its spatial distribution across the jet. Although no single definition exists, it can be expressed either in terms of velocity ratios or momentum fluxes [8]. A widely adopted formulation is based on the momentum ratio, which facilitates comparison across different configurations and operating conditions.

A variety of passive and active techniques have been employed to introduce swirl flow motions. Passive methods include guided vanes, tangential air injection, and rotating perforated plates [2, 3]. On the other side, active methods often rely on flow actuators such as dielectric barrier discharge plasma actuators (DBD-PAs) [9]. Passive systems are mechanically simple and energy-independent but lack real-time controllability and show optimal performances only for the design condition, while showing sub-optimal, if not detrimental, effects at any other operative conditions. In contrast, active devices can modulate the swirl strength, offering new possibilities in both open- and closed-loop flow control. Of course, the energy expenditure for their operation needs to be accounted for in efficiency evaluations.

This study focuses on comparing passive and active swirl generation methods in terms of their ability to induce and sustain a swirling motion in a round jet flow. The primary emphasis is placed on passive swirl generators composed of helical inserts designed to produce specified swirl numbers. A single active configuration using DBD-PAs is also presented for comparison. The objective is twofold: first, to assess the swirl number resulting from each configuration using stereoscopic particle image velocimetry (S-PIV); second, to evaluate the reliability of the proposed swirl number evaluation method by comparing the measured values against known design parameters.

The outcomes of this work are intended to provide a solid experimental basis for the characterization of swirl-induced flows. In particular, the validated methodology for the swirl number estimation offers a useful tool for assessing flow configurations where the swirl number is not known a priori, such as in the case of active flow control systems. Although an active configuration is considered for reference, the emphasis of this work lies on passive methods. The detailed analysis of their effects on the flow field - including velocity distribution, swirl generation, and spatial development — forms the foundation for subsequent investigations into active flow control strategies, where the same methodology can be extended to characterize flows with unknown or dynamically varying swirl intensity.

2 Experimental Setup

The present study investigates the three-dimensional velocity field of a swirling jet using stereoscopic particle image velocimetry. This section describes the experimental apparatus, operating conditions, and swirl generation strategies employed in the measurements.

2.1 Jet Facility

The jet facility featured a nozzle design developed to allow the rapid and flexible installation of different inserts, including a short pipe with a length-to-diameter ratio of 2.8, as well as both passive and active swirl generators. The converging section of the nozzle was shaped according to the Vitoshinski profile [10], to ensure a smooth acceleration of the flow and a uniform velocity profile across the exit section.

To control the flow conditions, static pressure taps were installed at both the inlet and the exit sections of the nozzle, enabling tests at a fixed pressure drop.

Compressed dry air was supplied through a pneumatic line. For S-PIV measurements, a Laskin nozzle (PIVlight30, PIVTEC GmbH) was installed between the pneumatic line supply and the jet facility to introduce seeding particles (PIVLIGHT, PIVTEC GmbH) into the airflow and ensure a uniform distribution within the measurement region.

2.2 S-PIV Setup and Data Processing

The S-PIV system consisted of two Andor Zyla ZL41 sCMOS cameras (5.5 Mpx, 2560×2160 px^2 sensor size) and a dual-cavity Nd:YAG laser (Dantec Dynamics, 15 Hz, 200 mJ/pulse). Each camera was equipped with a Tokina 100 mm macro lens ($f/2.8$D), a 532 nm optical bandpass filter to reduce the ambient light illumination, and a LaVision GmbH Scheimpflug adapter to ensure optimal focus across the entire measurement plane. The laser beam was shaped into a thin light sheet (approximately 1 mm thick) using a combination of spherical lenses ($f = -75$ mm and $f = 100$ mm) and a cylindrical lens

($f = -50$ mm). The laser and cameras were synchronized using a National Instruments PCI-6602 board. The measurement planes were positioned orthogonally to the jet axis.

The image-object calibration was performed using a double-plane target with a dot pattern and applying a pinhole camera model. A self-calibration procedure [11] was subsequently conducted to refine camera alignment, reducing the error to below 0.9 px.

Pre-processing of the raw images was carried out using a POD-based filtering algorithm [12], which proved effective in mitigating reflections and suppressing background noise.

Image processing and velocity vector computation were performed using the PaIRS-UniNa software suite [13, 14, 15, 16, 17, 18, 19, 20]. A multi-pass cross-correlation algorithm was applied, with final interrogation windows of 16×16 px^2 and 50% overlap. The image resolution was approximately 48.32 px/mm, resulting in a spatial vector resolution of about 6 vectors/mm.

The measured velocity fields feature Cartesian components along the horizontal (x) and vertical (y) axes and along the jet axis (z), defined by the mentioned geometric calibration. The corresponding velocity components are referred to as u, v and w, respectively. Nonetheless, most of the results shown in the next section consider the velocity fields projected on cylindrical coordinates: the radial (r), the tangential (θ) and the axial (z) directions. Correspondingly, these lead to the radial (V_r), azimuthal (V_θ) and axial (w) velocity components. Finally, it should be mentioned that all the flow statistics that are shown in this manuscript are time-averaged over 500 instantaneous realizations.

2.3 Swirl Generation Techniques

Both passive and active swirl generation methods were considered. This section offers a brief description of their characteristics.

2.3.1 Passive Swirl Generators The passive swirl generators were designed using helical vanes embedded in cylindrical inserts, which guided the flow along a spiral path. Three configurations corresponding to design (denoted with the subscript d) swirl numbers $S_\mathrm{d} = 0.1$, 0.2, and 0.3 were selected. The vane geometry was derived from the formulation proposed in [3] and is illustrated in Figure 1.

The swirl angle (Φ) was computed using the vane design equation, and the resulting helix pitch height (h) allowed the calculation of the number of revolutions (R) over a fixed axial length (L). Table 1 reports the key geometric parameters for each case.

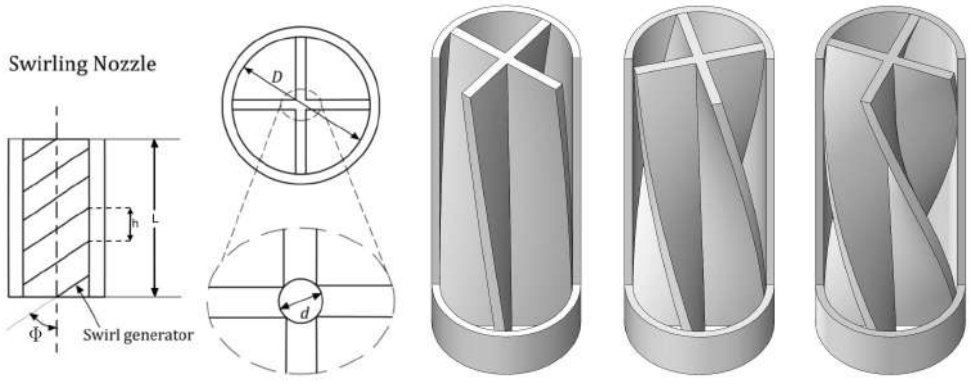

Figure 1: Passive swirl generators: (a) Geometrical definition ([21]); (b–d) inserts with $S_\mathrm{d} = 0.1$, $S_\mathrm{d} = 0.2$, and $S_\mathrm{d} = 0.3$.

2.3.2 Active swirl generators The active swirl generation system adopted in this study follows the configuration proposed in [9], where the swirl is induced by an array of surface-mounted DBD-PAs. Four DBD-PAs were installed along the axial length of a short pipe and evenly spaced around its circumference (i.e. one PA every 90 degrees of the nozzle circular crown). This arrangement was designed to impart a tangential velocity component to the flow without introducing mechanical obstructions or pressure losses, allowing for active modulation of the swirl intensity.

$S_\mathbf{d}$	L [mm]	D [mm]	d [mm]	$\tan(\Phi)$	R
0.1	70	25	2.83	0.1483	0.1038
0.2	70	25	2.83	0.2966	0.2076
0.3	70	25	2.83	0.4449	0.3114

Table 1: Geometric parameters of passive swirl generators

The passive swirlers were fabricated using 3D printing with PLA filament, with a wall thickness of 1.5 mm that served as the dielectric barrier. Each actuator was composed of two copper tape electrodes (0.35 mm thick): the exposed electrode, 3 mm wide and 50 mm long, was positioned on the inner surface in contact with the flow, while the encapsulated electrode, 5 mm wide and 50 mm long, was placed externally and insulated using three layers of Kapton tape.

The actuators were powered simultaneously using a high-voltage supply unit (Minipuls 4, GBS Elektronik GmbH). This system uses a full-bridge converter to produce a low-voltage square wave, which is stepped up by a transformer cascade to generate a sinusoidal waveform with a peak voltage of up to 20 kV. The input signal is driven by a DC power supply (Voltcraft VSP-2410) and a signal generator (RS PRO AFG-21005).

When the high voltage is applied, the air molecules adjacent to the exposed electrode become partially ionized and are accelerated towards the encapsulated electrode by the exerted Coulomb force [22, 23]. The resulting movement of ions within the electric field induces a localized flow — commonly referred to as an *ionic wind* — that imparts momentum to the surrounding fluid. This additional momentum generates a tangential velocity component in the main jet, effectively producing a controlled swirling motion. In this work, the active swirl configuration was tested at a peak-to-peak voltage of $V_{\mathrm{pp}} = 12$ kV and a frequency of 15 kHz. This voltage amplitude was chosen as a trade-off between the need to enable the active swirlers with some control authority, which suggests higher voltages, and to preserve the actuators from dielectric failures, which instead caps the supplied voltage amplitude. A 3D representation of the active swirler is shown in Figure 2.

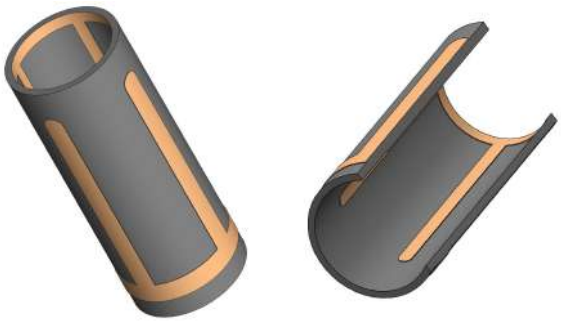

(a) (b)

Figure 2: Active swirl generator: (a) external view, (b) internal cross-section highlighting the electrode configuration.

3 Results

This section presents the key findings of the study. All measurements were conducted under a constant pressure drop (ΔP) of $\Delta P = 25.8$ Pa across the nozzle, which, in the axisymmetric jet configuration, resulted in an exit velocity, in the jet potential core, of 7.26 m/s and a corresponding reference Reynolds number, based on the jet bulk velocity and on the pipe outlet diameter (Re_b), of $Re_b \approx 1.2 \times 10^4$.

3.1 Swirl Number Evaluation

The flow actual swirl number (S) was evaluated at the streamwise location of $z/D = 0.5$, i.e. close to the nozzle exit, using the following expression, as reported in [9]:

$$S = \frac{\int_0^{2\pi} \int_0^{r_{max}} V_\theta(r,\theta)\, w(r,\theta) \cdot r^2 \, \mathrm{d}r \, \mathrm{d}\theta}{r_{max} \int_0^{2\pi} \int_0^{r_{max}} w(r,\theta)^2 \cdot r \, \mathrm{d}r \, \mathrm{d}\theta} \tag{1}$$

where r_{max} is the maximum measured radial position. Given the different flow structures induced by passive and active swirl generators, distinct procedures were employed to automatically identify the jet centre. In the case of the passive configurations, the centre was determined by scanning across the velocity field using a series of search windows and identifying the location at which the sum of the in-plane velocity components (u, v) reached a minimum. For the active configuration, where the axial velocity field exhibits a relatively uniform core, the jet centre was instead defined as the centroid of the central region showing nearly constant axial velocity.

Figure 3 displays the normalized mean velocity fields (w, V_r, V_θ) at $z/D = 0.5$ for each configuration, with the detected jet perimeter and centre also indicated with red lines and dot, respectively. Jets generated by means of passive swirlers exhibit a clear rotational structure in the tangential velocity component, with increasing intensity and coherence as S_d increases (see subplots (a.3), (b.3), and (c.3) in Figure 3). This trend is also reflected in the radial velocity maps, where alternating inflow and outflow lobes become more pronounced with stronger swirl. In contrast, the active configuration shows a substantially weaker and less organized rotational pattern, with the tangential and radial components largely confined to the jet boundary (see subplots (d.2), and (d.3) in Figure 3). The jet centre and perimeter are correctly identified in all configurations, as evidenced by their consistent placement within the flow field, further supporting the reliability of the detection method.

The computed swirl numbers are summarized in Table 2. Two main conclusions can be drawn from the results. First, the methodology used for swirl number computation is robust: in the passive cases, a good proximity is observed between the target (design) and the experimentally estimated values. Second, the swirl intensity induced by the DBD-based active configuration is notably lower than that obtained with passive swirlers, despite operating at relatively high voltage.

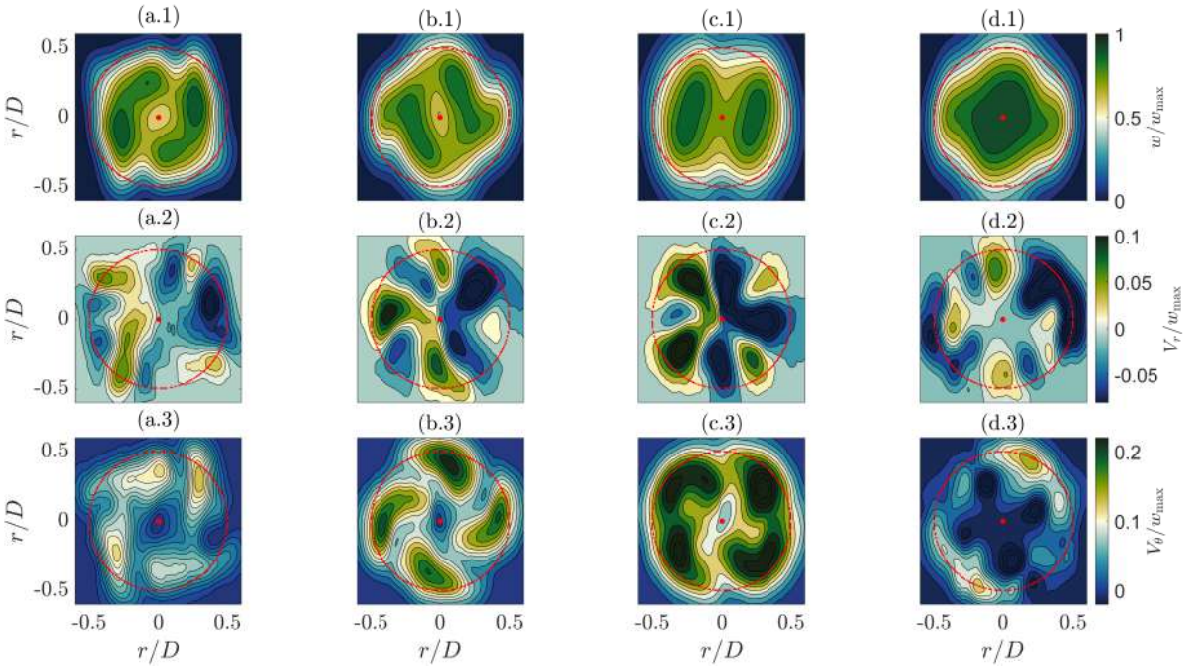

Figure 3: Mean axial, radial, and tangential velocity components normalized by w_max at $z/D = 0.5$ for: (a) $S_\mathrm{d} = 0.1$, (b) $S_\mathrm{d} = 0.2$, (c) $S_\mathrm{d} = 0.3$, and (d) active swirler; row 1: w/w_{max}, row 2: V_r/w_{max}, row 3: V_θ/w_{max}.

Swirl Generation Method	**Case**	**Swirl Number (S)**
Guided Vanes	$S_\mathrm{d} = 0.1$	0.1107
	$S_\mathrm{d} = 0.2$	0.2059
	$S_\mathrm{d} = 0.3$	0.2858
DBD-PAs	$V_\mathrm{pp} = 12$ kV	0.0821

Table 2: Calculated swirl numbers at $z/D = 0.5$ for passive and active configurations.

3.2 Mean Quadrant and Radial Distribution

Due to the intrinsic non-uniformity of the velocity fields, particularly in the case involving DBD-PAs, where asymmetries are likely attributed to the handcrafted nature of the device, a quadrant-averaged approach was adopted. The velocity field was divided into four angular sectors of 90°, and the velocity components were averaged within each quadrant to obtain a representative mean distribution.

Figure 4 shows the normalized quadrant-averaged velocity fields, referenced to the maximum axial velocity w_max recorded in each case. This normalization allows for a consistent qualitative comparison across the different swirl configurations.

Inspection of the radial and tangential components reveals broader and more intense high-velocity regions in the passive swirl configurations, particularly at the highest swirl number (Figure 4.c), compared to the active DBD-PA case (Figure 4.d). These patterns are in line with the swirl number results: the enhanced tangential velocity induced by the passive vanes significantly contributes to the numerator in Equation 1, thus increasing the swirl number. In contrast, although the DBD-PAs impart a swirling motion, their effectiveness appears limited under the tested operating conditions, resulting in a weaker tangential velocity field.

To quantitatively compare the various configurations, radial profiles were extracted from the quadrant-averaged fields. These profiles were obtained by azimuthally averaging the velocity components at each radial location within the mean quadrant.

In terms of axial velocity distribution (Figure 5.a), the axisymmetric jet exhibits a classical top-hat profile, with a nearly uniform velocity in the potential core region. In contrast, swirling jets exhibit a

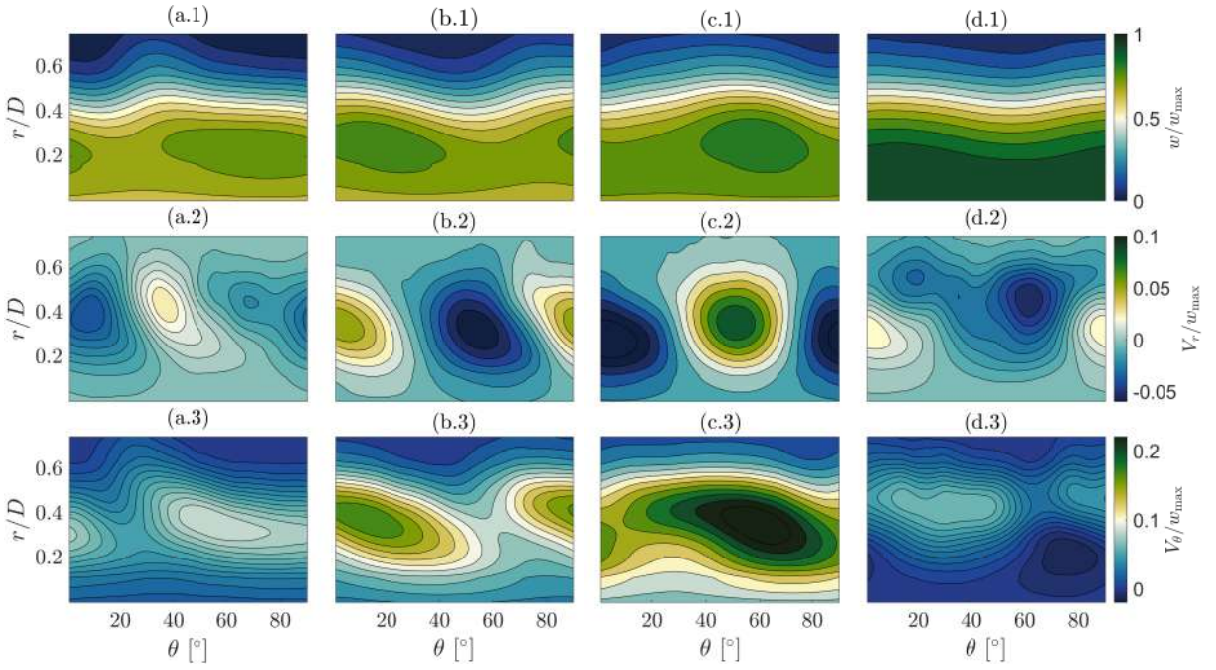

Figure 4: Quadrant-averaged velocity fields normalized by w_max for: (a) $S_\mathrm{d} = 0.1$, (b) $S_\mathrm{d} = 0.2$, (c) $S_\mathrm{d} = 0.3$, (d) active swirler; row 1: w/w_{max}, row 2: V_r/w_{max}, row 3: V_θ/w_{max}.

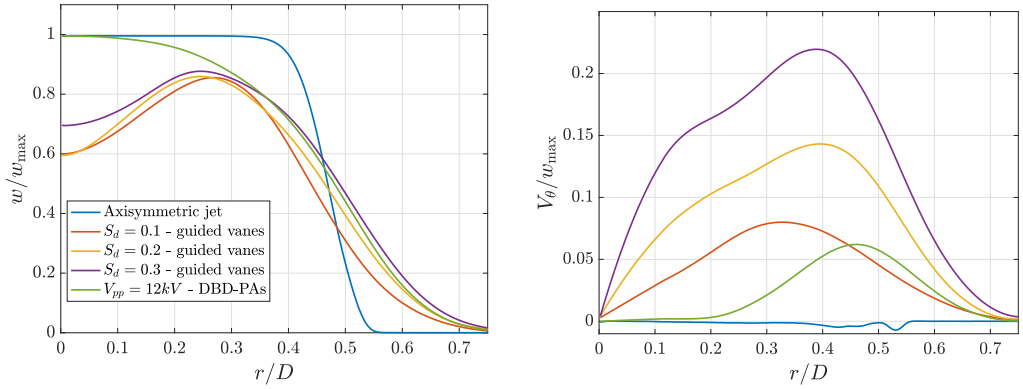

Figure 5: Normalized radial profiles of: (a) axial velocity $w/w_{\max}$; (b) tangential velocity $V_\theta/w_{\max}$

distinctly different behaviour, with the velocity peak occurring at an off-axis radial position. For passive swirl generators, the axial velocity decreases near the jet axis ($r/D = 0$), with the maximum occurring in the radial interval $0.2 < r/D < 0.3$. In the case of DBD-PAs, however, the peak remains centred on the axis and decreases gradually with increasing radial distance. Furthermore, both swirl generation methods lead to a broader axial velocity profile compared to the axisymmetric jet, highlighting the enhanced radial spreading induced by the swirl.

A similar trend is observed in the tangential velocity component (Figure 5.b). For the axisymmetric case, as expected, the tangential velocity is negligible across the entire radial domain. The passive swirl configurations exhibit a well-distributed azimuthal component that spans almost the entire radius, with peak values shifting outward as the swirl number increases. On the other hand, the active swirl case shows a localized tangential velocity distribution, with a lower peak value located between $r/D = 0.4$ and 0.5, corresponding to the radial position of the actuator electrodes. This suggests that the swirling motion generated by the DBD-PAs is concentrated near the swirler walls and does not significantly influence the central core of the jet.

3.3 Vorticity Fields

The azimuthal vorticity ω_z, computed using the expression below, was evaluated to further assess the flow's rotational structures induced by the different swirl generation strategies.

$$\omega_z = \left(\frac{\partial v}{\partial x} - \frac{\partial u}{\partial y} \right) \tag{2}$$

Figure 6 displays the normalized vorticity fields $\tilde{\omega}_z$ for all configurations, obtained by multiplying ω_z by $D/w_{\max}$. The comparison highlights notable differences between passive and active swirl generation mechanisms. In the passive cases, as the swirl number increases, the characteristic four-lobe structures become progressively less distinguishable due to increased overlap and interaction, eventually forming a more continuous swirling pattern. This behaviour reflects a stronger and more uniformly distributed rotational effect throughout the jet cross-section.

In contrast, the vorticity field associated with the active swirl configuration retains a well-defined four-lobe pattern, with limited interaction between adjacent vortical structures. This observation suggests that the swirling motion induced by the plasma actuators remains localized and primarily confined to the vicinity of the swirler walls, where the actuators are positioned.

This conclusion is further supported by examining the superimposed velocity vectors: in the passive cases - particularly for $S_\mathrm{d} = 0.2$ and $S_\mathrm{d} = 0.3$ — the swirling motion is distributed across the entire cross-section, extending from the jet-axis outwards. Conversely, in the active case, the vectors reveal four distinct zones of rotation, each centred around a DBD-PA, with limited cross-interaction. This confirms that the active method results in more isolated and confined vortical structures, emphasizing the localized influence of the actuators.

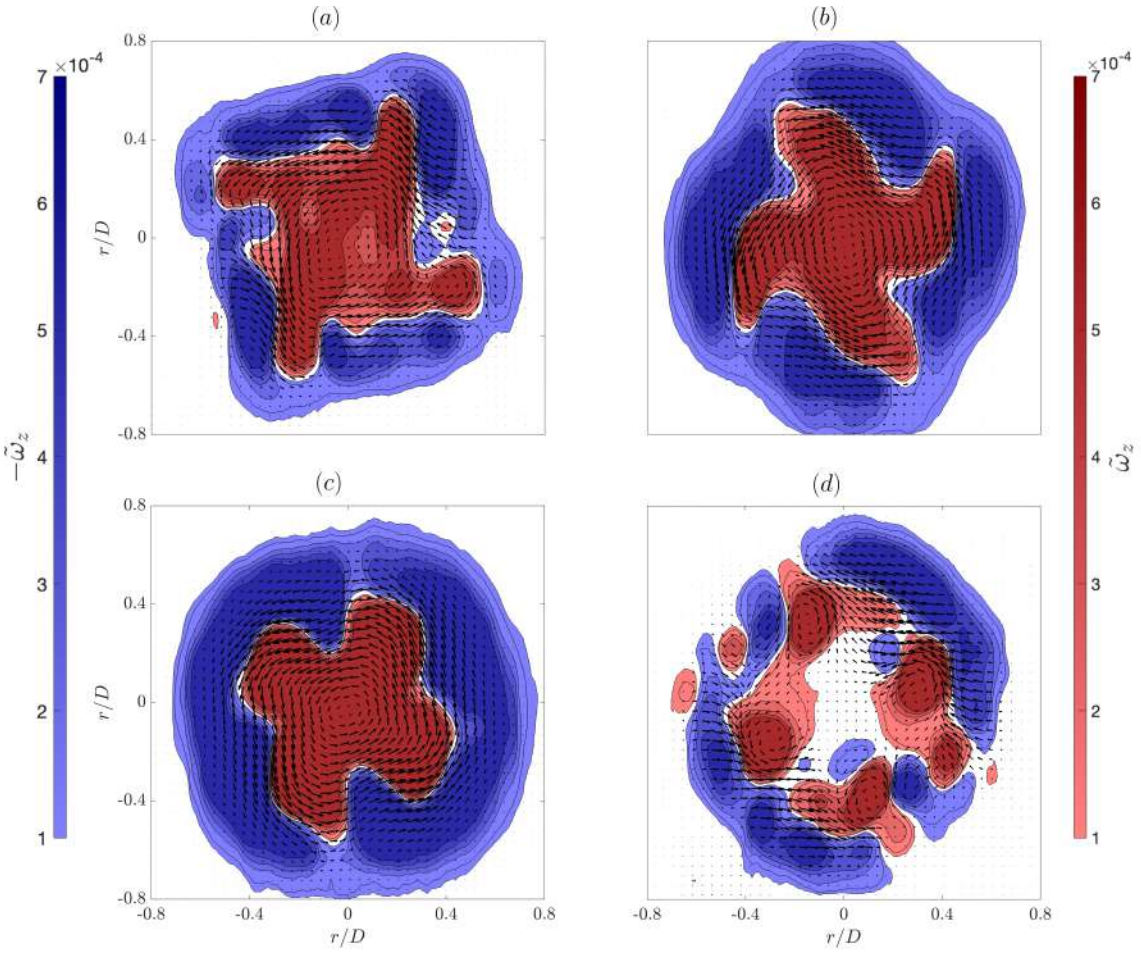

Figure 6: Velocity vectors and normalized vorticity fields at $z/D = 0.5$ (one vector plotted every 6 for clarity). - Passive swirl generators: (a) $S_\mathrm{d} = 0.1$, (b) $S_\mathrm{d} = 0.2$, and (c) $S_\mathrm{d} = 0.3$ (d) active swirler.

3.4 Three-Dimensional Flow Field Topology

To characterize the evolution of the jets along the axial direction, S-PIV measurements were conducted at multiple downstream locations. Specifically, eleven measurement planes were acquired at intervals of 12.5 mm — corresponding to half the injector diameter — covering a total axial distance from 0 mm to 125 mm from the exit section. Following post-processing, the velocity fields were interpolated to reconstruct a three-dimensional flow field for each configuration.

3.4.1 Axial Velocity Figure 7 illustrates the three-dimensional structure of the axial velocity component for the various swirl configurations. The isosurfaces correspond to $w/w_\mathrm{max} = 0.5$, thereby delineating regions where the axial velocity reaches half of its peak value for each case. Superimposed cross-sectional contours, extracted at several axial locations, offer further insight into the velocity distribution and the spatial evolution of the jet.

Consistent with the results reported in [24], the use of passive swirl generators induces a pronounced azimuthal asymmetry in the velocity distribution near the nozzle exit. Within approximately one diameter from the exit section, the flow exhibits a helical pattern due to the action of the guiding vanes. This results in a reduction of axial velocity near the jet centre and a corresponding increase in the peripheral regions. As the swirl number increases, a widening tendency can be observed and the four jets emerging from the four vanes remain distinct over a longer axial range. In the lowest swirl case ($S_\mathrm{d} = 0.1$), these jets coalesce more rapidly, and the velocity field assumes a more axisymmetric profile, similar to that of a non-swirling jet.

In contrast, the configuration utilizing active swirl generation via DBD plasma actuators produces

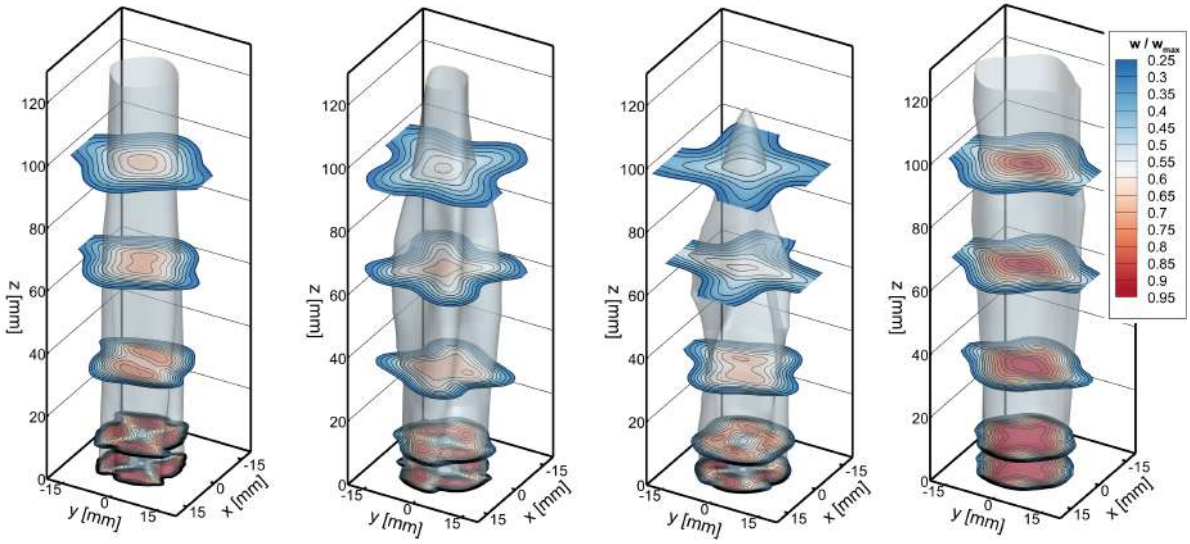

(a) (b) (c) (d)

Figure 7: Three-dimensional visualization of the time-averaged axial velocity component. Passive swirl generators: (a) $S_\mathrm{d} = 0.1$, (b) $S_\mathrm{d} = 0.2$, (c) $S_\mathrm{d} = 0.3$; (d) active swirler. The isosurfaces correspond to $w/w_\mathrm{max} = 0.5$.

an isosurface that retains a nearly axisymmetric shape throughout the measurement domain. No significant radial expansion or azimuthal deformation is observed, further confirming the lower swirl intensity achieved by the active method under the tested conditions.

3.4.2 Tangential Velocity The axial velocity analysis is further complemented by the investigation of the tangential velocity component, which provides a clearer distinction between the passive and active swirl strategies. As previously discussed, the guided vanes of the passive swirl generators impart a significant and spatially extensive tangential velocity field across the jet cross-section. This difference becomes even more evident in Figure 8, which shows the three-dimensional evolution of the azimuthal velocity component. The isosurfaces, set at $V_\theta/w_\mathrm{max} = 0.09$, delineate regions of appreciable rotational motion, while the accompanying cross-sections highlight the distribution of tangential velocity at selected downstream locations.

In the passive cases, the isosurfaces appear more voluminous and persist further downstream. As the swirl number increases, the tangential structures become more intertwined, reflecting the increased rotational energy and enhanced azimuthal momentum imparted by the vanes. These structures often interact with each other, forming a more complex flow topology as the flow develops.

In stark contrast, the active swirl configuration generates a much more confined tangential velocity field. The isosurface remains localized near the nozzle wall—where the DBD actuators are positioned—and dissipates rapidly, vanishing within approximately two diameters from the exit. This localization confirms that the effect of the plasma actuators is limited both spatially and in intensity, supporting the earlier observations on the relatively low swirl numbers achieved in this configuration.

3.4.3 Mass Flow Rate One of the key motivations for employing swirling jets lies in their enhanced entrainment capability compared to non-swirling configurations. To quantify this effect, the mass flow rate ($\dot{m}$) was evaluated along the jet axis for all tested configurations, providing an additional metric to compare the performance of the swirl generation methods.

The mass flow was calculated at each axial location following this equation:

$$\dot{m}(z) = \int_0^{2\pi} \int_0^{r_{max}} \rho\, w(r,\theta,z)\, r\, \mathrm{d}r\mathrm{d}\theta \tag{3}$$

where ρ is the air density.

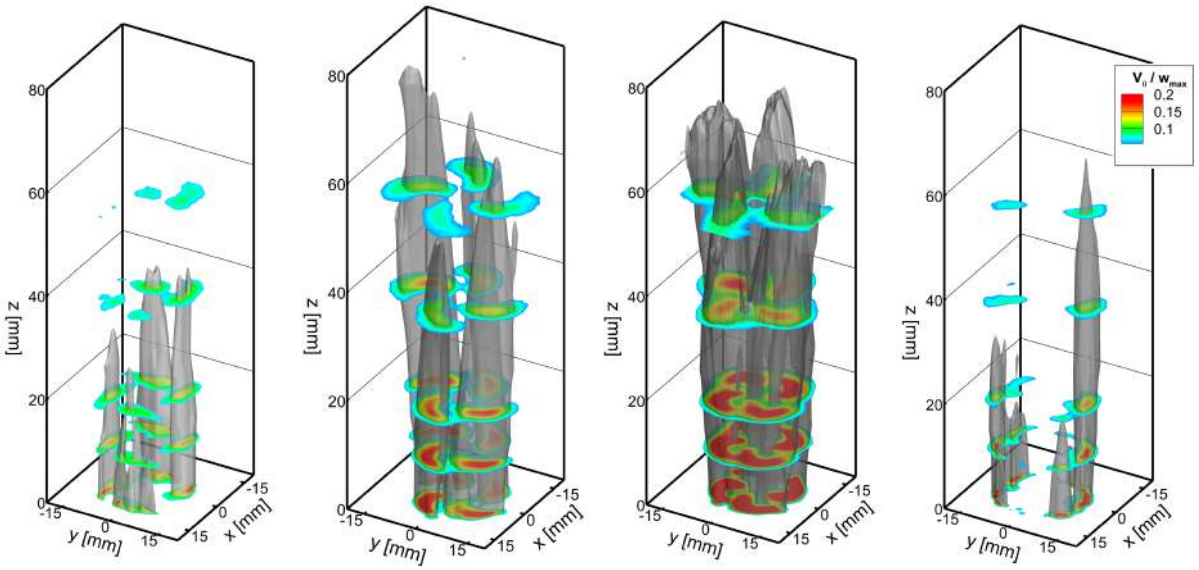

Figure 8: Three-dimensional visualization of the time-averaged tangential velocity component. Passive swirl generators: (a) $S_\mathrm{d} = 0.1$, (b) $S_\mathrm{d} = 0.2$, (c) $S_\mathrm{d} = 0.3$; (d) active swirler. The isosurfaces correspond to $V_\theta / w_\mathrm{max} = 0.09$.

Figure 9 presents the evolution of the normalized mass flow rate $\dot{m}(z)/\dot{m}_0$ as a function of the axial distance from the nozzle exit, where $\dot{m}_0 = \dot{m}(z = 0)$ denotes the mass flow rate at the nozzle exit section. Since the experimental setup does not include a flow meter, this normalization allows for a consistent comparison of the entrainment behaviour across different test cases, compensating for possible variations in the initial flow conditions.

The results corroborate the findings discussed in previous sections. Passive swirl generators exhibit a clear trend of increasing mass flow rate with downstream distance, and this effect becomes more pronounced as the design swirl number S_d increases — consistent with the enhanced entrainment typically associated with swirling flows -. In contrast, the active configuration based on DBD-PAs shows a milder growth in $\dot{m}/\dot{m}_0$, closely resembling the behaviour of a non-swirling jet. This suggests that, under the tested conditions, the momentum addition provided by the plasma actuators is insufficient to produce significant entrainment enhancement downstream.

4 Conclusions

In this study, stereoscopic particle image velocimetry was employed to experimentally characterize the velocity field of swirling jets generated through both passive and active methods. Particular attention was devoted to the quantification of the swirl number and the analysis of how the swirling motion develops and interacts with the jet flow in the near-field region.

The results clearly emphasize the differences between the two swirl generation strategies. Passive generators based on guided vanes showed a well-defined and persistent swirling motion. The tangential velocity component was broadly distributed across the jet cross-section, with an evident impact on both the velocity and vorticity fields. Conversely, the active configuration based on the installation and operation of an array of dielectric barrier discharge plasma actuators (DBD-PAs) generated a weaker swirling motion, confined primarily near the swirler walls and dissipating rapidly within two diameters from the pipe outlet. The evaluation of the induced swirl numbers from both passive and active methodologies showed that only the smallest design swirl number could be approached with the plasma-based swirler.

Despite these limitations, the results suggest that DBD-PAs remain a promising tool for imparting swirl, particularly due to their compactness and real-time controllability. The reduced performance observed in this study is not attributed to the actuation principle itself, but rather to two key factors: the constraints imposed by the dielectric material used for the injector-which limited the applicable voltage levels owing to failures of the dielectric when higher voltages were supplied—and the straight-electrode

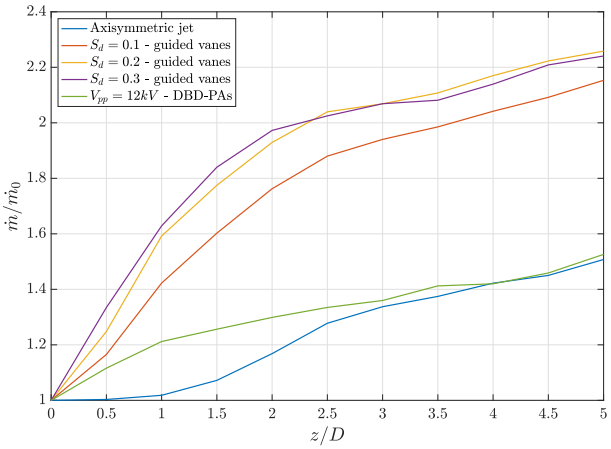

Figure 9: Normalized mass flow rate $\dot{m}/\dot{m}_0$ as a function of axial distance from the nozzle.

geometry of the DBD-PAs. Unlike guided vanes, which impart a continuous and constant azimuthal flow deflection along the jet axis, streamwise lain down DBD actuators apply a localized and constant circumferential forcing only at their electrode positions. This fundamental difference in flow deflecting likely contributes to the more confined and rapidly decaying swirl observed with plasma actuation.

Future work should focus on optimizing the active configuration by adopting alternative dielectric materials - such as quartz glass - which would enable operation at higher voltages, and by exploring alternative actuator designs, such as helical-shaped electrodes as proposed in [25]. These improvements could enhance the induced momentum and improving the effectiveness of the swirling motion, paving the way for more robust and tunable active swirl generation techniques, with potential applications in flow control and combustion systems.

References

[1] Chigier N, Beèr JM. 1964 Velocity and Static-Pressure distributions in swirling air jets issuing from annular and divergent nozzles. *Journal of Basic Engineering* **86**, 4, 788–796. (doi:10.1115/1.3655954).

[2] Chigier N, Chervinsky A. 1967 Experimental investigation of swirling vortex motion in jets. *Journal of Applied Mechanics* **34**, 2, 443–451. (doi:10.1115/1.3607703).

[3] Gupta AK, Lilley DG, Syred N. 1984 Swirl flows. *International Journal of Heat and ,Mass Transfer* **28**, 5, 1055. (doi:doi.org/10.1016/0017-9310(85)90288-1).

[4] Lucca-Negro O, O'Doherty T. 2001 Vortex breakdown: a review. *Progress in energy and combustion science* **27**, 4, 431–481. (doi:10.1016/S0360-1285(00)00022-8).

[5] Syred N, Beer JM. 2017 Combustion in swirling flows: A review. *Journal of physics. Conference series* **891**, 12237–. (doi:10.1016/0010-2180(74)90057-1).

[6] Billant P, Chomaz JM, Huerre P. 1998 Experimental study of vortex breakdown in swirling jets. *Journal of fluid mechanics* **376**, 183–219. (doi:10.1017/s0022112098002870).

[7] Ceglia G, Discetti S, Ianiro A, Michaelis D, Astarita T, Cardone G. 2014 Three-dimensional organization of the flow structure in a non-reactive model aero engine lean burn injection system. *Experimental Thermal and Fluid Science* **52**, 164–173. (doi:10.1016/J.EXPTHERMFLUSCI.2013.09.007).

[8] Toh IK, Honnery D, Soria J. 2010 Axial plus tangential entry swirling jet. *Experiments in Fluids* **48**, 2, 309–325. (doi:10.1007/s00348-009-0734-2).

[9] Li G, Jiang X, Zhao Y, Liu C, Chen Q, Xu G, Liu F. 2017 Jet flow and premixed jet flame control by plasma swirler. *Physics letters. A* **381**, 13, 1158–1162. (doi:10.1016/j.physleta.2017.01.060).

[10] Levenhagen J. 2017 Converging nozzle design in an anechoic wind tunnel. *University of Florida* .

[11] Wieneke B. 2008 Volume self-calibration for 3D particle image velocimetry. *Experiments in Fluids* **45**, 4, 549–556. (doi:10.1007/s00348-008-0521-5).

[12] Mendez MA, Raiola M, Masullo A, Discetti S, Ianiro A, Theunissen R, Buchlin JM. 2017 Pod-based background removal for particle image velocimetry. *Experimental thermal and fluid science* **80**, 181–192. (doi:10.1016/j.expthermflusci.2016.08.021).

[13] Astarita T, Cardone G. 2005 Analysis of interpolation schemes for image deformation methods in piv. *Experiments in Fluids* **38**, 2, 233–243. (doi:10.1007/s00348-004-0902-3).

[14] Astarita T. 2006 Analysis of interpolation schemes for image deformation methods in piv: effect of noise on the accuracy and spatial resolution. *Experiments in Fluids* **40**, 6, 977–987. (doi:10.1007/s00348-006-0139-4).

[15] Astarita T. 2007 Analysis of weighting windows for image deformation methods in piv. *Experiments in Fluids* **43**, 6, 859–872. (doi:10.1007/s00348-007-0314-2).

[16] Astarita T. 2008 Analysis of velocity interpolation schemes for image deformation methods in piv. *Experiments in Fluids* **45**, 2, 257–266. (doi:10.1007/s00348-008-0475-7).

[17] Astarita T. 2009 Adaptive space resolution for piv. *Experiments in Fluids* **46**, 6, 1115–1123. (doi:10.1007/s00348-009-0618-5).

[18] Giordano R, Astarita T. 2009 Spatial resolution of the stereo piv technique. *Experiments in Fluids* **46**, 4, 643–658. (doi:10.1007/s00348-008-0589-y).

[19] Paolillo G, Astarita T. 2020 Perspective camera model with refraction correction for optical velocimetry measurements in complex geometries. *IEEE Transactions on Pattern Analysis and Machine Intelligence* **44**, 6, 3185–3196. (doi:10.1109/TPAMI.2020.3046467).

[20] Paolillo G, Astarita T. 2021 On the piv/ptv uncertainty related to calibration of camera systems with refractive surfaces. *Measurement Science and Technology* **32**, 9, 094006. (doi:10.1088/1361-6501/abf3fc).

[21] Ianiro A, Cardone G. 2012 Heat transfer rate and uniformity in multichannel swirling impinging jets. *Applied thermal engineering* **49**, 89–98. (doi:10.1016/j.applthermaleng.2011.10.018).

[22] Kriegseis J, Simon B, Grundmann S. 2016 Towards in-flight applications? a review on dielectric barrier discharge-based boundary-layer control. *Applied mechanics reviews* **68**, 2. (doi:10.1115/1.4033570).

[23] Kotsonis M, Ghaemi S, Veldhuis L, Scarano F. 2011 Measurement of the body force field of plasma actuators. *Journal of physics. D, Applied physics* **44**, 4, 045204–045204. (doi:10.1088/0022-3727/44/4/045204).

[24] Ianiro A, Lynch KP, Violato D, Cardone G, Scarano F. 2018 Three-dimensional organization and dynamics of vortices in multichannel swirling jets. *Journal of fluid mechanics* **843**, 180–210. (doi:10.1017/jfm.2018.140).

[25] 2020 Design and experimental evaluation of a plasma swirler with helical shaped actuators. *Sensors and actuators. A. Physical.* **315**, 112250–. (doi:10.1016/j.sna.2020.112250).